Journal of
Materials Chemistry C

PAPER

View Article Online
View Journal | View Issue

Cite this: *J. Mater. Chem. C*, 2015, 3, 11449

Received 13th July 2015,
Accepted 5th October 2015

DOI: 10.1039/c5tc02115d

www.rsc.org/MaterialsC

Tunable plasmonic surfaces *via* colloid assembly†

T. Honold, K. Volk, A. Rauh, J. P. S. Fitzgerald and M. Karg*

Self-assembly of plasmonic colloids is a key challenge on the road to the cost-efficient fabrication of optically active surfaces. Here, we show that core–shell particles with plasmonic cores and hydrogel shells are ideal building blocks for coatings with engineered optical properties. The plasmonic properties of the colloids are tuned by selective overgrowth of the gold cores with either gold or silver shells of variable thicknesses. This library of particles is used for monolayer preparation by self-assembly at the air/water interface and subsequent transfer onto solid supports. These monolayers of hexagonally packed particles have very similar particle densities and center-to-center distances, independent of the metal core composition and size. Consequently, our simple and robust bottom-up approach allows us to precisely tailor the optical properties of solid surfaces.

Introduction

Optically functional coatings are critical to materials science with widespread applications in sensing,[1–7] photovoltaics[8–12] and metamaterials.[13–18] Ideal building blocks for such coatings are noble metal nanoparticles due to their ability to support localised surface plasmon resonances (LSPRs).[19–22] These LSPRs are collective oscillations of the conduction electrons, causing intense electromagnetic fields in close proximity to the nanoparticle.[2,23] The plasmon resonance position, width and intensity depend on the particle size, shape and composition, as well as on the refractive index of the surrounding medium.[24–26] Fortunately, the last several decades have seen tremendous progress in the synthesis of nanoparticles with precise control over these aspects,[27–31] and a broad toolbox of plasmonic particles with tailored resonances is readily available.

Several challenges limit the widespread use of colloidal plasmonic particles in optical devices: colloidal stability, structural control in assembly, processability, and availability. The first three are primarily the result of an uncontrolled surface chemistry, and the last is due to the low concentrations achievable in most metal nanoparticle synthesis protocols – usually in the nanomolar range. Furthermore, typical reduction protocols yield only particles of a single size and shape population.

A clever way to extend the range of optical properties available through wet-chemical synthesis of plasmonic colloids is the controlled overgrowth of preformed precursor particles. Such seeded-growth protocols allow further tuning of size and shape starting from seed particles.[32–34] Through this approach, a library of colloidal building blocks covering a broad range of optical properties (resonance position, width and number of resonances) is accessible.

In this work, we propose core–shell colloids with small, spherical gold cores and semi-transparent hydrogel shells as a convenient precursor material for seeded-growth and the realisation of plasmonic surfaces with tailored optical properties. The hydrogel encapsulation was realised by seeded precipitation copolymerisation of *N*-isopropylacrylamide (NIPAM) and *N*,*N*-methylenebisacrylamide (BIS) according to a well-established protocol.[35] The role of the hydrogel shell is threefold: (1) to ensure colloidal stability in aqueous dispersion and different organic solvents such as alcohols. (2) To control surface coverage upon assembly of the particles into, *e.g.*, a monolayer.[36] (3) To allow for diffusion-controlled overgrowth of the gold nanoparticle cores.[37–39]

We employed this strategy to generate a library of plasmonic core–shell particles with the same hydrogel shell and hydrodynamic diameter but with different plasmonic metal cores. Our synthetic protocol allows us to adjust precisely the absorbance and the LSPR position of our particles within a range of wavelengths as large as 100 nm. This is confirmed by simple Mie theory calculations. These particles were assembled at the air/water interface and subsequently transferred onto glass slides. The particle density and the hexagonal packing of the transferred particle arrays are found to be independent of the size and composition of the plasmonic cores. The particle packing is solely determined by the hydrogel shell. Consequently, monolayers with very similar particle densities but significantly different absorption/scattering ratios and LSPR peak wavelength were prepared. Such structures are easily fabricated in a fast, cost-efficient and reproducible manner on cm-scale substrates. Upscaling to larger sample sizes may become possible in a

Physical Chemistry I, University of Bayreuth, Universitaetsstr. 30, 95440 Bayreuth, Germany. E-mail: matthias.karg@uni-bayreuth.de; Web: www.karg.uni-bayreuth.de

† Electronic supplementary information (ESI) available. See DOI: 10.1039/c5tc02115d

roll-to-roll production approach.[40] Our plasmonic coatings are particularly interesting as light management structures in hybrid photovoltaic devices.[8]

Experimental section

Chemicals

Ascorbic acid (Aldrich, >99%), 3-butenylamine hydrochloride (Aldrich, 97%), cetyltrimethylammonium bromide (CTAB, Aldrich, >98%), cetyltrimethylammonium chloride (CTAC, Aldrich, 25 wt%, H_2O), ethanol (abs. VWR), glycine (Merck, >99.7%), H_2O_2 (VWR, 30%), *N*-isopropylacrylamide (Aldrich, 97%), *N*,*N*′-methylenebis(acrylamide) (Aldrich, 99%), NH_4OH_{aq} (Applichem, 25%), potassium peroxodisulfate (Merck, 99%), silver nitrate (Fluka, >99.5%), sodium dodecylsulfate (SDS, SERVA, 99%) and tetrachloroauric(III) acid (Aldrich, 99.999%) were used as received. Milli-Q water with a resistivity of 18.2 MΩ cm was used in all synthesis and purification procedures.

Synthesis

Precursor particles. The precursor particles were prepared following a previously published protocol.[35] In brief, citrate stabilised gold nanoparticles of approximately 20 nm in diameter were prepared according to the Turkevich method[41] and functionalised by the addition of butenylamine hydrochloride. The particles were purified and concentrated by centrifugation. The functionalised gold nanoparticles were encapsulated by hydrogel shells using a seeded precipitation polymerisation of *N*-isopropylacrylamide (0.06 M) and *N*,*N*-methylenebisacrylamide (15 mol% as referred to monomer) as cross-linker. The polymerisation was carried out at 70 °C for two hours. The core–shell particles were then purified by centrifugation and redispersion in water. The final purified product was freeze-dried.

Gold overgrowth. Au@Au–PNIPAM particles were obtained by using a modified surfactant assisted seeded-growth protocol in order to overgrow the gold nanoparticle cores of the precursor particles.[32] All overgrowth experiments were done using a constant molar ratio of ascorbic acid/$HAuCl_4$ of 1.3. At first, a precursor stock solution was prepared by diluting a 2 wt% solution of precursor particles with the same volume of a 100 mM CTAC solution. Next, a feed solution was prepared containing 0.5 mM $HAuCl_4$ and 4.75 mM CTAC. In a typical synthesis, 200 μL precursor stock solution was combined with 8 mL of a 2.4 mM CTAC solution under heavy stirring in a 20 mL glass vial, followed by the addition of 83 μL of a freshly prepared ascorbic acid solution (10 mM). Next, 1.280 mL feed solution was added dropwise to the seed solution under stirring. The reaction was allowed to proceed for 20 minutes. The particles were purified by centrifugation at 3740 rcf until the supernatant was colourless. The supernatant was discarded and the precipitate was redispersed in water. This process was repeated twice. The final core size of the particles was 30 nm as determined by transmission electron microscopy (TEM). Particles with overgrown gold cores of 41, 60 and 92 nm in diameter were obtained by adding 3.0, 6.7 and 29.3 mL feed solution to the precursor particles, respectively.

Silver overgrowth. Similar to the gold overgrowth, Ag@Au–PNIPAM particles were synthesised following a surfactant assisted protocol for overgrowth of the initial gold cores of the precursor particles with silver.[42] In a typical synthesis, 2.860 mL precursor particles were added to 10 mL of a 50 mM CTAB solution containing 400 mM glycine under heavy stirring. Next, 800 μL of a 0.1 M NaOH and 450 μL of a 100 mM freshly prepared ascorbic acid solution were added to the precursor particles. 1.31 mL of a 15 mM $AgNO_3$ feed solution was added dropwise to the seed solution and stirring was continued for 20 min. The particles were purified as described above. The final core size was 28 nm as determined by TEM. Larger cores were obtained by reducing the volume of precursor particles to 800 μL (46 nm cores), 146 μL (72.7 nm cores) and 50 μL (99.8 nm cores), respectively.

Monolayer preparation

Cleaning of glass slides. Microscope slides (Thermo Scientific) were cleaned by sonication in acetone, 2-propanol and water for 20 min each, followed by heating at 80 °C in a 1 : 1 : 5 mixture by volume of H_2O_2, NH_4OH_{aq} (25%) and H_2O for 30 min. Afterwards, the glass slides were cleaned with water several times and dried using nitrogen gas.

Assembly. All core–shell particles were assembled into monolayers at the air/water interface using a crystallising dish filled with a dilute, aqueous SDS solution (0.05 mM).[43] A clean glass slide was placed inside the crystallising dish at a tilt angle of approximately 30°. A concentrated particle dispersion was transferred into an Eppendorf tube, diluted with the same volume of EtOH and homogenised using a Vortexer. 0.1–0.2 mL of the dispersion were filled into a 1 mL syringe equipped with a 27G × 3/4″ cannula (0.4 × 20 mm). The water/ethanol solvent mixture was chosen in order to allow for spreading of the particle dispersion at the air/water interface. SDS was used below the critical micelle concentration. The surfactant acts as a soft blocking layer and facilitates the transfer of the monolayer on a solid support.[44] We adjusted the bulk concentrations of the particle dispersions between 1 and 2 wt%, depending on the size of the plasmonic core of the particles. The particle dispersion was steadily transferred *via* the glass slide onto the air/water interface, forming a freely floating monolayer. The monolayers were collected onto 1 cm^2 glass substrates. The substrates were immersed below the monolayer and withdrawn at a shallow angle, lifting out the floating particle monolayer. Immediately after withdrawal of the monolayer, the samples were carefully dried using a heat gun.

Characterisation

TEM. All core–shell particles were analysed by transmission electron microscopy (TEM) using a ZEISS CEM 902 TEM operating at an acceleration voltage of 80 kV. Samples were prepared by drop casting of highly dilute, aqueous particle dispersions on carbon coated copper grids (200 mesh). The dried samples were investigated in bright-field operation. Image analysis was done with the image processing software ImageJ, measuring the size of at least 100 different particles (metal cores) for each sample.

AFM. $10 \times 10\ \mu m^2$ AFM images were recorded with a Nanoscope Multimode AFM (Veeco) in tapping mode. The particle monolayers on glass substrates were measured at ambient conditions in air. OTESPA-R3 AFM probes (Bruker) with spring constants of approximately 26 N m^{-1} were employed. Only the height profiles were used for image analysis. All images were flattened (1st order) using the Nanoscope (Bruker) software. Nearest neighbour center-to-center distances were obtained using ImageJ.

SEM. The particle monolayers were investigated using scanning electron microscopy (SEM) with a ZEISS Ultra plus field emission scanning electron microscope (FE-SEM). The samples were vapour coated with approximately 30 nm of carbon using a Balzers Union MED 010 device. Images were recorded with an acceleration voltage between 2–10 kV using an in-lens and a SE2 detector to visualize the topography of the sample.

DLS and zeta potential. Dynamic light scattering (DLS) and zeta potential (ζ) experiments were performed on a NanoZS Zetasizer (Malvern Instruments) equipped with a 633 nm He–Ne laser at a detection angle of 173°. For all core–shell samples, dilute aqueous dispersions were measured at 25 °C. The samples were equilibrated for 10 minutes before acquisition of the correlation functions. For DLS experiments, three correlation functions were recorded for each sample using acquisition times of 60 seconds. The hydrodynamic diameters were obtained by Cumulant analysis provided by the instrument software. Electrophoretic mobilities were measured and calculated into ζ-potentials by the instrument software using the Einstein–Smoluchowski relation. Three consecutive measurements were performed for each sample.

UV-Vis extinction spectroscopy. All absorbance spectra were measured in a wavelength range of 190–1100 nm using an Agilent 8453 UV-Vis Spectrophotometer. Dilute aqueous dispersions of the core–shell particles were measured in quartz cells with 1 cm light path. Spectra of the particle monolayers were recorded using glass substrates as solid supports. All experiments were performed at ambient conditions.

Calculation of theoretical extinction spectra. Theoretical extinction spectra were calculated *via* Mie theory using Mathematica 10, following the multilayer recursive method.[45] Particle core dimensions were taken from TEM measurements, with a hydrogel shell diameter of 330 nm. Overgrown particles include a gold core with 20 nm in diameter. The refractive indices of gold and silver were taken from Johnson and Christy[46] and modified to include electron surface scattering at small sizes.[47] The refractive index of the hydrogel shell was given by a simple model of $n_{H_2O} + dn$, where n_{H_2O} is the refractive index of water,[48] and $dn = 0.05$ was the best fit value to the precursor particle absorption spectra. The host medium was water. Multipole expansions included 5–8 terms, such that all calculated wavelengths have less than 0.1% relative error.

Results and discussion

Au–PNIPAM precursor particles

To address the challenges of colloidal stability and control of particle–particle separation, we encapsulated plasmonic gold nanoparticles with rather thick hydrogel shells. This shelling procedure is based on a seeded precipitation polymerisation protocol.[35] The obtained core–shell precursor particles (Au–PNIPAM) have single gold nanoparticle cores of 20 nm in diameter as obtained by TEM and soft, cross-linked poly(*N*-isopropylacrylamide) (PNIPAM) shells. The overall hydrodynamic diameter of the core–shell particles dispersed in water is 325 nm as determined by DLS (25 °C, swollen state). Consequently, the swollen shell has a thickness on the order of 150 nm. The porous, highly swollen structure of the hydrogel allows diffusion of small molecules into the shell, so post-modification of the gold core is possible.

Overgrowth of the cores of the precursor particles

In order to achieve a whole toolbox of core–shell particles with different plasmonic properties but the same overall particle dimensions and interactions, we applied successive overgrowth of the precursor cores by gold and silver. This way we changed the diameter and composition of the cores starting from only one precursor system (Au–PNIPAM).

We used surfactant assisted seeded-growth protocols in combination with mild reducing conditions to guarantee homogeneous overgrowth of the gold precursor cores and suppress secondary nucleation. Previous studies have shown that the ratio of reactants, pH, temperature, concentration of the surfactant, and nature of the halide counter ion strongly influence the final nanoparticle morphology.[49,50] The surfactant cetyltrimethylammonium chloride (CTAC) was chosen for the gold overgrowth because it helps to suppress the formation of non-spherical geometries. Due to the presence of the surfactant, the redox potential of the metal salt is changed through complexation. Consequently, complete reduction takes place only at the metal surface when a mild reducing agent is used.[51] Control on the core size was achieved by adding increasing amounts of feed solution and the reducing agent ascorbic acid to the precursor particles. A similar protocol was used for the silver overgrowth, which was done under basic conditions (pH approx. 10) in order to increase the reducing strength of ascorbic acid.[52] The synthetic protocol was adjusted in order to get similar core sizes as for the Au@Au–PNIPAM particles by variation of the amount of seed particles.

The core–shell particles upon successive overgrowth of the precursor cores will be denoted Au*x*@Au20–PNIPAM and Ag*y*@Au20–PNIPAM throughout the rest of the manuscript. Here x (y) refers to the thickness of the gold (silver) shell, and Au20 refers to the initial gold core of 20 nm in diameter. For instance, Ag4@Au20–PNIPAM is a core–shell system with a 4 nm-thick silver shell, grown on the gold core with 20 nm in diameter. Therefore, the total core diameter of this example particle is 28 nm.

Fig. 1 shows schematic depictions of the structure of the different kinds of core–shell particles along with photographs of samples before overgrowth (Au–PNIPAM) and after progressive steps of gold growth (Au@Au–PNIPAM) as well as silver growth (Ag@Au–PNIPAM). The change in core size is clearly visible from the photographs. While the precursor particles appear as

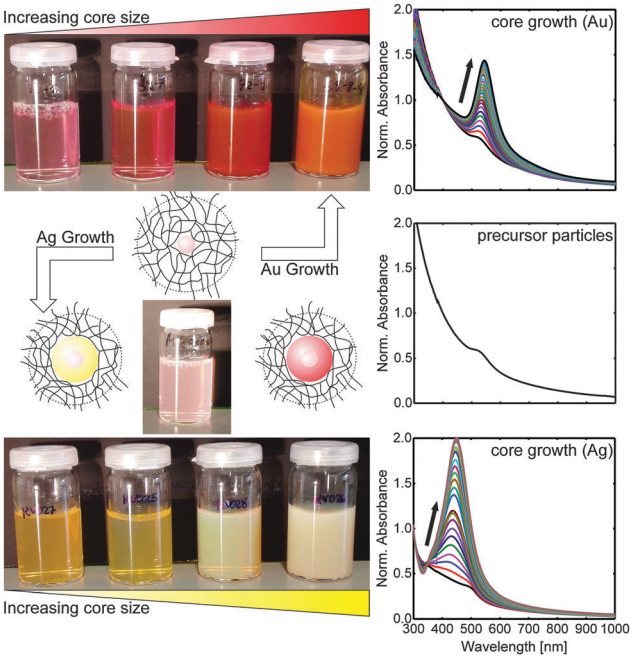

Fig. 1 Controlled overgrowth: the gold core of the initial core–shell particles, Au–PNIPAM, with gold cores of 20 nm in diameter (left column, middle) can be selectively overgrown with silver (bottom) or with gold (top) leading to an increase in core size. The respective absorbance spectra (right column) illustrate the changes of the optical properties during the overgrowth with silver (bottom) and with gold (top). The spectra were normalized to the absorbance at 400 nm (gold overgrowth) and at 300 nm (silver overgrowth).

a slightly red and turbid dispersion, the overgrown samples exhibit much stronger colour: red for gold and yellow for silver. This increase in colour intensity is related to the increasing absorption of the cores with larger sizes. At the same time, the photographs of the particle dispersions show that the scattering of the samples increases with the core size. This is the result of the increased scattering cross-section for the larger cores.

The optical impression from the photographs of the samples is confirmed by UV-Vis absorbance spectra shown in the right column of Fig. 1. The spectrum in the middle of the right column represents the absorbance of the precursor particles, Au–PNIPAM. The spectrum reveals a weak LSPR peak, originating from the gold cores, at approximately 523 nm. The strong scattering of the relatively large hydrogel shell dominates the spectrum. This is visible as an increase in absorbance for shorter wavelengths.[35]

The changes of the optical properties for the overgrown samples are entirely attributed to the scattering and absorption of the plasmonic cores because the hydrogel shell dimensions will be nearly unaffected by the core growth (see hydrodynamic diameter D_h in Table 1). When the precursor particles are overgrown, the absorption to scattering ratio changes, and the plasmonic properties become more pronounced (Fig. 1, right column, top and bottom). For both growth materials, Au and Ag, the plasmon resonance intensifies with increasing core size. Furthermore, the position of the plasmon resonance is affected by the overgrowth of the metal cores: for gold as growth material, a continuous shift of the plasmon resonance to longer wavelengths is observed for increasing core dimensions. For growth with silver, the plasmon resonance initially shifts to shorter wavelengths as compared to the initial Au–PNIPAM precursor particles. This is caused by the higher restoring force from the nuclei in silver as compared to gold. Upon growth of the silver shell the plasmon resonance shifts to longer wavelengths as the thickness of the silver shell increases. In order to better understand this transition, we synthesised four different metal shell thicknesses using gold and silver growth each aiming at comparable shell thicknesses for the two metals.

Table 1 Summary of the different plasmonic colloids prepared from core overgrowth of Au–PNIPAM precursor particles. The average core diameter D_{core} was obtained from size analysis of the TEM micrographs. λ_{LSPR}(Exp) denotes the position of the LSPR obtained from the UV-Vis measurements of aqueous particle dispersions and λ_{LSPR}(Mie) gives the LSPR position obtained from Mie calculation. D_h is the hydrodynamic diameter of the particles and ζ denotes the zeta potential, both measured in water at 25 °C

Sample	D_{core} [nm]	λ_{LSPR}(Exp) [nm]	λ_{LSPR}(Mie) [nm]	D_h [nm]	ζ [mV]
Au–PNIPAM	20 ± 2	523	530	325	−17.3
Au5@Au20–PNIPAM	30 ± 4	532	532	325	−17.3
Au10@Au20–PNIPAM	41 ± 5	532	531	315	−2.9
Au20@Au20–PNIPAM	60 ± 7	540	541	316	−4.2
Au36@Au20–PNIPAM	92 ± 12	561	568	316	−1.1
Ag4@Au20–PNIPAM	28 ± 3	—	380	336	−11.5
Ag13@Au20–PNIPAM	46 ± 3	433	437	317	−6.8
Ag26@Au20–PNIPAM	73 ± 5	458	464	329	−9.3
Ag40@Au20–PNIPAM	100 ± 6	496	503	336	−9.6

Fig. 2 shows TEM images of the whole set of synthesised particles, including the precursor particles (a). The spherical gold nanoparticles of the precursor particles are clearly visible as circles of much higher contrast (black) as compared to the PNIPAM-shell (grey). Note that each precursor particle contains only one gold core. The TEM micrographs in Fig. 2b–e show the particles after overgrowth with gold. The diameter of the spherical cores is clearly increasing from (b) to (e). This way, gold shell thicknesses between 5 and 36 nm are accessible, corresponding to total core sizes of 30 to 92 nm. This range of sizes is significantly larger as compared to the ones realized in a previous work where we performed overgrowth of already adsorbed particles (monolayer by spin-coating).[37] Furthermore, much better control on the particle morphology upon overgrowth was achieved in the present work. Non-spherical side products and secondary nucleation were not observed. Similar overgrowth results were obtained with silver, as can be seen by the TEM micrographs j–m in Fig. 2. Spherical particles with silver shell thicknesses of 4 to 40 nm closely match the results of the gold overgrowth. The core dimensions from TEM analysis are listed in Table 1.

The ensemble absorbance spectra of the Au@Au–PNIPAM and Ag@Au–PNIPAM particles in aqueous dispersion are plotted in Fig. 2f–i. For comparison, spectra of Au@Au–PNIPAM and Ag@Au–PNIPAM colloids of similar core sizes are plotted in the same graphs along with theoretical extinction spectra. Additionally, the absorbance of the Au–PNIPAM precursor particles is included in each graph (blue solid lines). The spectra are normalised to the absorbance at 400 nm for an easier comparison.

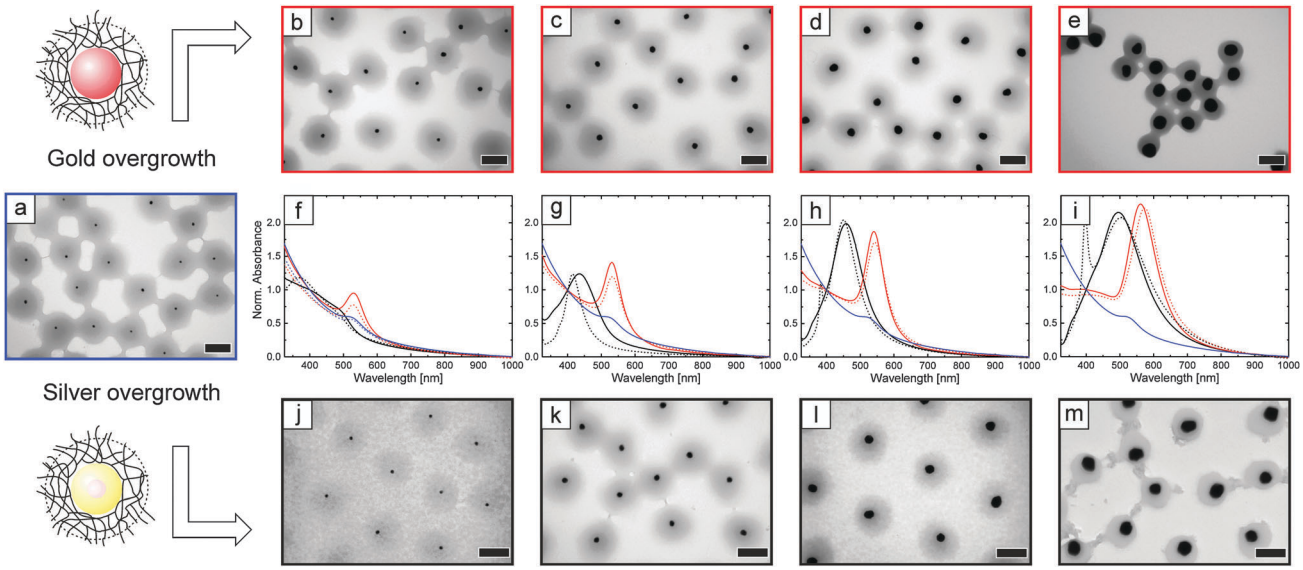

Fig. 2 Microscopic and spectroscopic characterization of the plasmonic particles after different steps of core growth. (a) TEM image of the initial precursor particles, Au–PNIPAM. (b)–(e) TEM micrographs after overgrowth with gold. (j)–(m) TEM micrographs after overgrowth with silver. All scale bars in the TEM images correspond to 100 nm. The average core diameters of the Au@Au–PNIPAM particles are 30 nm (b), 41 nm (c), 60 nm (d) and 92 nm (e) and 28 nm (j), 46 nm (k), 73 nm (l), and 100 nm (m) for Ag@Au-PNIPAM. (f)–(i) UV-Vis absorbance spectra for the precursor particles (blue solid lines), the Au@Au–PNIPAM particles (red solid lines) and the Ag@Au–PNIPAM particles (black solid lines). Spectra for similar overall core sizes after overgrowth with gold and silver are plotted in one diagram for comparison. The dashed lines are theoretically calculated extinction spectra obtained by Mie theory.

Almost all samples show a pronounced, single extinction peak that is attributed to the dipolar LSPR of the metal cores, with the exception of the precursor and the smallest overgrown silver particles. The small half width of the resonances manifests the low polydispersity of our particles despite several steps of sequential overgrowth. The absence of any other plasmonic modes further highlights that the core overgrowth did not produce any non-spherical particle morphologies as side products.

Having a closer look at the LSPR peak positions, a change from 523 to 561 nm is observed for gold as growth material. The resonance red shifts and the absorbance at the resonance increases with increasing core size. For silver as growth material a slightly different behaviour is observed for the first step of core growth. Overgrowth with a 4 nm-thick silver shell broadens and blue shifts the local absorbance maximum as compared to the LSPR of the initial Au–PNIPAM colloids. A clear LSPR peak cannot be clearly determined. This can be attributed to a synergistic effect between the two metals, where the gold core induces significant damping due to the mismatch of the dielectric function of the bimetallic core.[53] Increasing the silver shell further to 13 nm leads to a significant change of the optical properties and a clear LSPR peak is now detectable. This LSPR is significantly blue shifted (by 90 nm) as compared to the Au–PNIPAM particles. For these particles, the bimetallic cores behave optically very similar to pure silver spheres due to the low volume fraction of the gold core (8%) and shallow skin depth of the surface plasmon. With a further increase in the silver shell thickness, the LSPR shifts to longer wavelength and becomes more intense. The LSPR positions of all particles with Ag@Au cores lie in a range of 433–496 nm. The LSPR wavelengths, λ_{LSPR}, of all samples are summarised in Table 1. The observed peak wavelengths of the resonances agree well with results from literature.[32]

Theoretical extinction spectra of spherical particles with core dimensions from TEM analysis are included in Fig. 2 as dotted lines. A very good match between the experimental and the calculated spectra is found for all core–shell particles with gold cores, including the Au–PNIPAM precursor particles. Table 1 shows that both sets of spectra provide nearly identical positions of the LSPR maximum, except for Au36@Au20–PNIPAM. In the latter case, small deviations of the spherical shape of these particles could explain the difference between the two LSPR positions. Simulations of Ag26@Au20–PNIPAM and Ag40@Au20–PNIPAM particles also match closely to the ensemble spectra. However, the simulated quadrupolar mode at 382 nm (Ag26@Au20–PNIPAM) and at 398 nm (Ag40@Au20-PNIPAM) is not observable in the experimental spectra. We attribute this to an irregular morphology of the silver shell in the overgrown particles. In Fig. 2m, the faceted character of the polycrystalline particles explains the deviation of the simulated spectra, which assume an ideal spherical geometry of the nanoparticles. In the case of Ag13@Au20–PNIPAM, simulation and experimental spectra differ significantly. An anisotropic growth of the silver shell or slight variation of core sizes could explain the observed deviations, which are even more pronounced for the Ag4@Au20–PNIPAM particles. We attribute this to the synergistic effect of the gold and silver as discussed above.

Plasmonic monolayer *via* colloidal assembly

In the next step, we used our library of core–shell colloids for the assembly into ordered monolayers. Our particles are mostly stabilised by steric interactions. The surface charge, stemming from the anionic radical initiator used in the shell growth, is

small and slightly negative. Zeta potentials measured in aqueous dispersion at 25 °C reveal only small changes of the surface charge when the core size is changed (see Table 1) which might be a result of incomplete removal of CTAB or CTAC used in the core growth. Thus, we expect very similar particle–particle interactions for the whole series of particles independent of the core dimensions. For the assembly, particle dispersions in a 1 : 1 mixture (by volume) of H_2O and ethanol were floated at the air/water interface, as described in the Experimental section.[43] However, we want to stress here that the freely floating monolayer did not cover the whole accessible surface area of the air/water interface, which is rather different as compared to typical interface assemblies as realized in, *e.g.*, a Langmuir trough. After immersing the particles at the interface, the spontaneously formed monolayers were transferred onto glass substrates by gentle lifting. Upon transfer onto glass slides, the monolayers were investigated by AFM and UV-Vis spectroscopy. AFM images were always recorded with different scan sizes and at completely independent, random sample positions. We did not find any significant deviation on the degree of order nor on the inter-particle distances at different sample positions. Representative results from these measurements are presented in Fig. 3. In addition, SEM images of the monolayer samples shown in Fig. 3a–d and i–l can be found in the ESI,† Fig. S1–S8. Images a–d show selected 10 × 10 μm^2 AFM height profiles of Au@Au–PNIPAM arrays on glass, and similarly i–l the profiles of Ag@Au–PNIPAM arrays. Additionally, digital photographs of the particle monolayers on glass slides of approximately 1 cm^2 are included as insets in Fig. 3a–d and i–l. The photographs show homogeneous coverage over the whole substrates as evident from the strong iridescence colours. As can be seen from the AFM images, all particles assembled into highly ordered, hexagonally packed monolayers. Large ordered domains are observable. Furthermore, a clear separation between the particles is found. This is related to the shrinkage of the previously highly swollen hydrogel shell upon drying of the monolayer. The particle density and nearest neighbour distance d_{c-c} of the monolayers are summarised in Table 2.

All monolayers have comparable particle densities with an average of 4.65 particles per μm^2 and values of d_{c-c} in the order of 460 nm. The inter-particle distance is large compared to the average hydrodynamic diameter of 323 nm of the particles measured with DLS (Table 2). This points to an anisotropic deformation of the hydrogel shell at the interface as has been observed previously for purely organic hydrogel particles adsorbed at a liquid/liquid interface.[54] Since all monolayers show very similar values of d_{c-c} and very regular, hexagonal packing of the particles independent on the size and composition of the

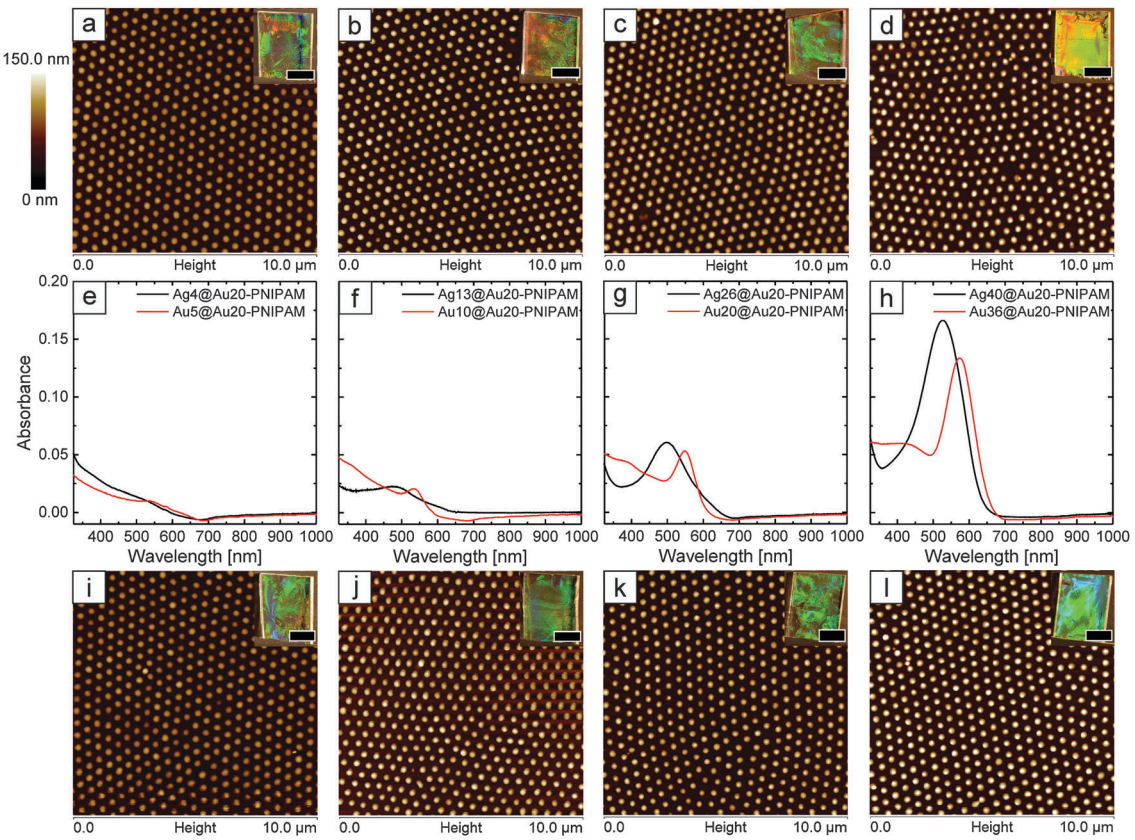

Fig. 3 Characterization of Au@Au–PNIPAM and Ag@Au–PNIPAM monolayers. (a)–(d) Tapping mode AFM height profiles of Au@Au–PNIPAM particles. (e)–(h) UV-Vis spectra of the monolayers on glass. Spectra of Au@Au–PNIPAM and Ag@Au–PNIPAM arrays with comparable core sizes are combined in one graph (a&i, b&j, c&k and d&l). (i)–(l) AFM height profiles of Ag@Au–PNIPAM arrays. The insets show digital photographs of the monolayers on glass slides of approximately 1 cm^2. The scale bars correspond to 5 mm.

Table 2 Analysis of particle monolayers. Center-to-center distances (d_{c-c}) and particle densities (ρ) were obtained from the AFM height profiles using ImageJ software. The LSPR positions (λ_{LSPR}) and absorbance values (Abs(λ_{LSPR})) were extracted from absorbance spectra of monolayers on glass

Sample	d_{c-c} [nm]	ρ [particles per μm^2]	λ_{LSPR} [nm]	Abs(λ_{LSPR})
Au5@Au20–PNIPAM	473 ± 15	4.49	—	—
Au10@Au20–PNIPAM	465 ± 14	4.76	536	0.02
Au20@Au20–PNIPAM	445 ± 15	4.94	547	0.053
Au36@Au20–PNIPAM	463 ± 19	4.45	573	0.133
Ag4@Au20–PNIPAM	461 ± 23	4.71	—	—
Ag13@Au20–PNIPAM	455 ± 22	4.77	484	0.022
Ag26@Au20–PNIPAM	453 ± 23	4.48	499	0.06
Ag40@Au20–PNIPAM	459 ± 20	4.67	527	0.166
Binary sample	455 ± 17	4.67	564	0.146

plasmonic metal core, it is obvious that only the hydrogel shell drives the particle assembly. In other words, interface assembly of our metal–hydrogel core–shell particles allows the fabrication of highly ordered monolayers with nearly the same surface coverage from Au@Au and Ag@Au nanoparticles covering a diameter range from 20 to 100 nm. Because the monolayer structure and density is nearly the same for all samples, we can now investigate the dependence of the optical properties on the core size and material using far-field extinction spectroscopy.

Fig. 3e–h show UV-Vis extinction spectra of the monolayers on glass. For comparison, the absorbance of Ag@Au–PNIPAM and Au@Au–PNIPAM monolayers with comparable sized cores are plotted in one graph. The spectra show very similar results as compared to those recorded in solution (Fig. 2). It is worth noting that the illuminated area on the substrates is the same for all samples and that the spectra shown in Fig. 3 were not normalised nor shifted. Therefore, we conclude that the increase in absorbance is solely related to the increasing core volume, since roughly the same number of particles is probed for each sample.

The determined LSPR peak positions and values of absorbance at the resonance are listed in Table 2. For the smallest core sizes (Fig. 3e) the weak LSPR signal is related to the small absorption and scattering cross-sections of these rather small metal nanoparticle cores. With increasing core size, the plasmonic properties of the samples become more pronounced.

Fig. 4a shows the dependence of the LSPR position (λ_{LSPR}) as a function of the metal shell thickness obtained after each step of core growth, both of the particles in solution and of the monolayers on glass. Because of the high sensitivity of the plasmon resonance to the local refractive index, the peak positions of the particle monolayers on glass are shifted to longer wavelengths for both types of particles.[26] This effect is stronger for the cores overgrown with silver. Furthermore, Fig. 4b shows that the absorbance of the different monolayers increases with the plasmonic shell thickness of the overgrown cores, independent of the growth material, *i.e.*, silver and gold. For both sets of samples, the maximum shell thicknesses exhibit an absorbance increase by almost a factor of 10. This nicely underlines that our colloidal library not only allows the fabrication of plasmonic coatings with tailored resonance positions but also the tuning of the absorbance and consequently transmission of the monolayer.

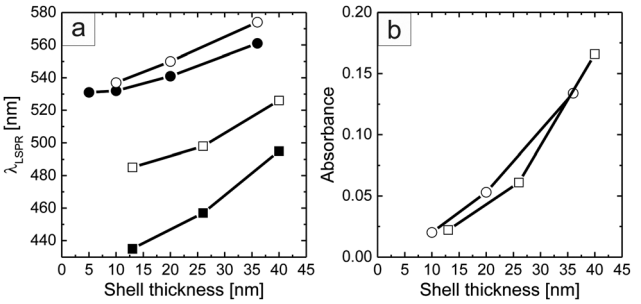

Fig. 4 Results from analysis of the UV-Vis absorbance spectra. (a) LSPR peak wavelength, λ_{LSPR}, and (b) absorbance at the LSPR maximum as a function of the shell thickness obtained after sequential overgrowth of the gold cores of the precursor particles. Results are shown for spectra measured from aqueous dispersions (filled symbols) and monolayers on glass (open symbols) and for Au@Au–PNIPAM (circles), and Ag@Au–PNIPAM (squares).

Mixed monolayer

To further demonstrate the tunability of the optical properties of our self-assembled particle arrays, we prepared a 1 : 1 mixed monolayer (by weight) of Ag40@Au20–PNIPAM and Au36@Au20–PNIPAM particles. Fig. 5a and b show an AFM height profile and a FE-SEM image of the binary monolayer, respectively. The

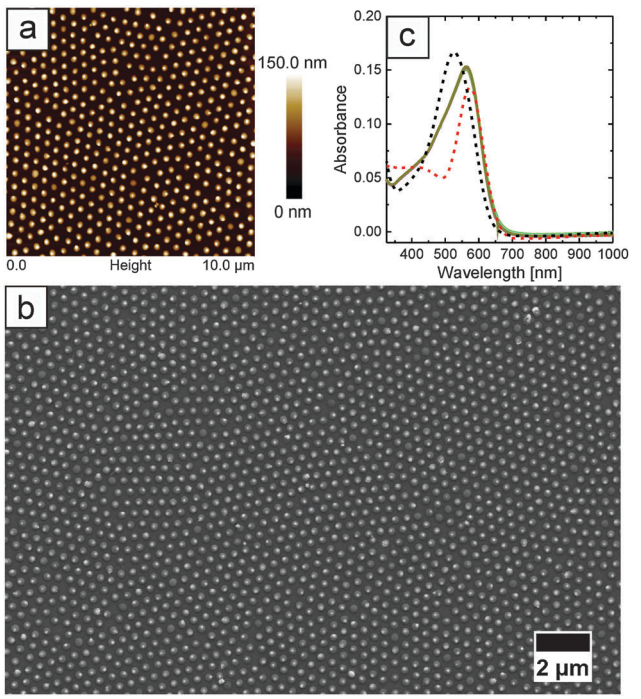

Fig. 5 Mixed particle monolayer on glass prepared from a 1 : 1 mixture (by weight) of Ag40@Au20–PNIPAM and Au36@Au20–PNIPAM particles. (a) AFM height profile, (b) FE-SEM image of the mixed monolayer, (c) UV-Vis absorbance spectra measured at five different positions of the sample (solid lines). Note, that the spectra look almost identical. For comparison, the absorbance of Ag40@Au20–PNIPAM (black dashed line) and Au36@Au20–PNIPAM (red dashed line) monolayers are included.

images indicate homogeneous surface coverage and an ordered packing of the particles, very similar to the monolayers of single core species shown in Fig. 3. The average particle center-to-center distance of 452 ± 19 nm is similar to the previously discussed monolayers. Due to their same hydrodynamic dimensions (see Table 1) and hydrogel shell morphology, particles assemble into ordered structures with inter-particle distances and order parameters independent of the plasmonic core size and composition.

Fig. 5c shows absorbance spectra of the mixed monolayer recorded at five different positions of the sample. The spectra match very nicely which manifests the random but homogeneous distribution of the Ag@Au–PNIPAM and Au@Au–PNIPAM particles throughout the whole monolayer.

Additionally, the absorbance spectra of monolayers prepared from the single systems, Ag40@Au20–PNIPAM (black dotted line) and Au36@Au20–PNIPAM (red dotted line), are included in the diagram for comparison. The peak wavelength and absorbance of the mixed monolayer are in between the properties of the individual colloidal building blocks. Thus, blending of Ag@Au–PNIPAM and Au@Au–PNIPAM particles is a quick and easy technique to further tune the absorption and scattering properties of the particle arrays.

Conclusions

With this work, we provide an experimental example of easily fabricated, macroscopic, plasmonic monolayers with controlled surface coverage, where the plasmonic properties are systematically varied through the chemical pre-treatment (core overgrowth) of one type of colloidal core–shell building blocks. Seeded growth was applied as a versatile protocol to tune the dimensions, composition, and hence, the optical properties of the plasmonic cores with almost nanometre precision. Our synthetic protocol based on Au–PNIPAM core–shell colloids produces neither secondary nucleation nor non-spherical side products, allowing the synthesis of a library of monodisperse, spherical metal particles with core sizes ranging from 20 to 100 nm in diameter. Furthermore, self-assembly at the air/water interface was applied as a sophisticated technique that allows for surface patterning with highly ordered particle monolayers. This approach works for all the particles in our library. The obtained monolayers have uniform surface coverage and inter-particle distances. Due to the difference in core size and composition, we can adjust the LSPR position of the monolayers between 484 and 573 nm by the choice of the building blocks. We demonstrated that blending of core-shell particles with different cores is easily possible, providing another handle on optically fine tuning the plasmonic properties of colloidal coatings. In the future, reducing the hydrogel shell dimensions of the core–shell particles may allow for the realization of smaller inter-particle separations in the monolayer. In this case, plasmon resonance coupling might be usable as another parameter to tune the plasmonic properties of the monolayer.

Acknowledgements

MK and TH acknowledge financial support *via* the Deutsche Forschungsgemeinschaft (DFG) through the SFB 840. MK, JPSF, and KV are grateful for financial support *via* the Deutsche Forschungsgemeinschaft (DFG) through the Emmy Noether programme. The authors acknowledge Markus Retsch from the University of Bayreuth (Physical Chemistry I) for fruitful discussion and assistance with the interface assembly and Martina Heider (BIMF, University of Bayreuth) for her assistance with the FE-SEM investigations.

References

1 C. Hamon, S. Novikov, L. Scarabelli, L. Basabe-Desmonts and L. M. Liz-Marzan, *ACS Nano*, 2014, **8**, 10694–10703.
2 K. A. Willets and R. P. Van Duyne, *Annu. Rev. Phys. Chem.*, 2007, **58**, 267–297.
3 A. J. Haes, C. L. Haynes, A. D. McFarland, G. C. Schatz, R. R. Van Duyne and S. L. Zou, *MRS Bull.*, 2005, **30**, 368–375.
4 M. E. Stewart, C. R. Anderton, L. B. Thompson, J. Maria, S. K. Gray, J. A. Rogers and R. G. Nuzzo, *Chem. Rev.*, 2008, **108**, 494–521.
5 N. Vogel, M. Jung, N. L. Bocchio, M. Retsch, M. Kreiter and I. Köper, *Small*, 2010, **6**, 104–109.
6 T. Thai, Y. Zheng, S. H. Ng, S. Mudie, M. Altissimo and U. Bach, *Angew. Chem., Int. Ed.*, 2012, **51**, 8732–8735.
7 M. Mueller, M. Tebbe, D. V. Andreeva, M. Karg, R. A. Alvarez Puebla, N. Pazos Perez and A. Fery, *Langmuir*, 2012, **28**, 9168–9173.
8 M. Karg, T. A. F. König, M. Retsch, C. Stelling, P. M. Reichstein, T. Honold, M. Thelakkat and A. Fery, *Mater. Today*, 2015, **18**, 185–205.
9 H. Choi, J. P. Lee, S. J. Ko, J. W. Jung, H. Park, S. Yoo, O. Park, J. R. Jeong, S. Park and J. Y. Kim, *Nano Lett.*, 2013, **13**, 2204–2208.
10 H. L. Gao, X. W. Zhang, Z. G. Yin, H. R. Tan, S. G. Zhang, J. H. Meng and X. Liu, *Appl. Phys. Lett.*, 2012, **101**, 133903.
11 H. A. Atwater and A. Polman, *Nat. Mater.*, 2010, **9**, 205–213.
12 P. Reineck, G. P. Lee, D. Brick, M. Karg, P. Mulvaney and U. Bach, *Adv. Mater.*, 2012, **24**, 4750–4755.
13 D. Chanda, K. Shigeta, S. Gupta, T. Cain, A. Carlson, A. Mihi, A. J. Baca, G. R. Bogart, P. Braun and J. A. Rogers, *Nat. Nanotechnol.*, 2011, **6**, 402–407.
14 O. Hess, J. B. Pendry, S. A. Maier, R. F. Oulton, J. M. Hamm and K. L. Tsakmakidis, *Nat. Mater.*, 2012, **11**, 573–584.
15 W. Lewandowski, M. Fruhnert, J. Mieczkowski, C. Rockstuhl and E. Gorecka, *Nat. Commun.*, 2015, **6**, 1–9.
16 C. M. Soukoulis and M. Wegener, *Nat. Photonics*, 2011, **5**, 523–530.
17 Z. H. Jiang, S. Yun, F. Toor, D. H. Werner and T. S. Mayer, *ACS Nano*, 2011, **5**, 4641–4647.
18 Q. Q. Gan, F. J. Bartoli and Z. H. Kafafi, *Adv. Mater.*, 2013, **25**, 2385–2396.

19 M. Arnold, V. C. Hirschfeld-Warneken, T. Lohmüller, P. Heil, J. Blümmel, E. A. Cavalcanti-Adam, M. López-García, P. Walther, H. Kessler, B. Geiger and J. P. Spatz, *Nano Lett.*, 2008, **8**, 2063–2069.
20 L. Jiang, C. Zou, Z. Zhang, Y. Sun, Y. Jiang, W. Leow, B. Liedberg, S. Li and X. Chen, *Small*, 2014, **10**, 609–616.
21 M.-H. Lin, H.-Y. Chen and S. Gwo, *J. Am. Chem. Soc.*, 2010, **132**, 11259–11263.
22 A. Tao, P. Sinsermsuksakul and P. Yang, *Nat. Nanotechnol.*, 2007, **2**, 435–440.
23 S. Linic, P. Christopher and D. B. Ingram, *Nat. Mater.*, 2011, **10**, 911–921.
24 P. Mulvaney, *Langmuir*, 1996, **12**, 788–800.
25 L. M. Liz-Marzan, *Langmuir*, 2006, **22**, 32–41.
26 C. Novo, A. M. Funston, I. Pastoriza-Santos, L. M. Liz-Marzan and P. Mulvaney, *J. Phys. Chem. C*, 2008, **112**, 3–7.
27 M. Grzelczak, J. Perez-Juste, P. Mulvaney and L. M. Liz-Marzan, *Chem. Soc. Rev.*, 2008, **37**, 1783–1791.
28 T. K. Sau and A. L. Rogach, *Adv. Mater.*, 2010, **22**, 1781–1804.
29 R. Sardar, A. M. Funston, P. Mulvaney and R. W. Murray, *Langmuir*, 2009, **25**, 13840–13851.
30 M. Rycenga, C. M. Cobley, J. Zeng, W. Li, C. H. Moran, Q. Zhang, D. Qin and Y. Xia, *Chem. Rev.*, 2011, **111**, 3669–3712.
31 S. J. Tan, M. J. Campolongo, D. Luo and W. Cheng, *Nat. Nanotechnol.*, 2011, **6**, 268–276.
32 J. Rodríguez-Fernández, J. Pérez-Juste, F. J. García de Abajo and L. M. Liz-Marzán, *Langmuir*, 2006, **22**, 7007–7010.
33 N. Pazos-Perez, F. J. Garcia de Abajo, A. Fery and R. A. Alvarez-Puebla, *Langmuir*, 2012, **28**, 8909–8914.
34 N. R. Jana, L. Gearheart and C. J. Murphy, *J. Phys. Chem. B*, 2001, **105**, 4065–4067.
35 M. Karg, S. Jaber, T. Hellweg and P. Mulvaney, *Langmuir*, 2011, **27**, 820–827.
36 S. Jaber, M. Karg, A. Morfa and P. Mulvaney, *Phys. Chem. Chem. Phys.*, 2011, **13**, 5576–5578.
37 M. B. Muller, C. Kuttner, T. A. F. Konig, V. V. Tsukruk, S. Forster, M. Karg and A. Fery, *ACS Nano*, 2014, **8**, 9410–9421.
38 R. Contreras-Caceres, J. Pacifico, I. Pastoriza-Santos, J. Perez-Juste, A. Fernandez-Barbero and L. M. Liz-Marzan, *Adv. Funct. Mater.*, 2009, **19**, 3070–3076.
39 J. Clara-Rahola, R. Contreras-Caceres, B. Sierra-Martin, A. Maldonado-Valdivia, M. Hund, A. Fery, T. Hellweg and A. Fernandez-Barbero, *Colloids Surf., A*, 2014, **463**, 18–27.
40 N. Vogel, S. Goerres, K. Landfester and C. K. Weiss, *Macromol. Chem. Phys.*, 2011, **212**, 1719–1734.
41 J. Turkevich, P. C. Stevenson and J. Hillier, *Discuss. Faraday Soc.*, 1951, **11**, 55–75.
42 R. Contreras-Caceres, I. Pastoriza-Santos, R. A. Alvarez-Puebla, J. Perez-Juste, A. Fernandez-Barbero and L. M. Liz-Marzan, *Chem. – Eur. J.*, 2010, **16**, 9462–9467.
43 N. Vogel, C. Fernández-Lopez, J. Párez-Juste, L. M. Liz-Marzán, K. Landfester and C. K. Weiss, *Langmuir*, 2012, **28**, 8985–8993.
44 M. Retsch, Z. Zhou, S. Rivera, M. Kappl, X. S. Zhao, U. Jonas and Q. Li, *Macromol. Chem. Phys.*, 2009, **210**, 230–241.
45 A. Moroz, *Ann. Phys.*, 2005, **315**, 352–418.
46 P. B. Johnson and R. W. Christy, *Phys. Rev. B: Solid State*, 1972, **6**, 4370–4379.
47 C. F. Bohren and D. R. Huffman, *Absorption and Scattering of Light by Small Particles*, Wiley-VCH Verlag GmbH, 2007.
48 G. M. Hale and M. R. Querry, *Appl. Opt.*, 1973, **12**, 555–563.
49 S. E. Lohse, N. D. Burrows, L. Scarabelli, L. M. Liz-Marzán and C. J. Murphy, *Chem. Mater.*, 2014, **26**, 34–43.
50 M. R. Langille, M. L. Personick, J. Zhang and C. A. Mirkin, *J. Am. Chem. Soc.*, 2012, **134**, 14542–14554.
51 J. Rodriguez-Fernandez, J. Perez-Juste, P. Mulvaney and L. M. Liz-Marzan, *J. Phys. Chem. B*, 2005, **109**, 14257–14261.
52 B. Rodriguez-Gonzalez, A. Burrows, M. Watanabe, C. J. Kiely and L. M. Liz-Marzan, *J. Mater. Chem.*, 2005, **15**, 1755–1759.
53 M. Tebbe, C. Kuttner, M. Mayer, M. Maennel, N. Pazos-Perez, T. A. F. König and A. Fery, *J. Phys. Chem. C*, 2015, **119**, 9513–9523.
54 K. Geisel, L. Isa and W. Richtering, *Langmuir*, 2012, **28**, 15770–15776.